nature communications

Article

https://doi.org/10.1038/s41467-026-75717-y

Real-time photoactivated SRS imaging enables spatiotemporally controlled nitroxyl release and therapeutic guidance in vivo

Received: 29 January 2026

Accepted: 7 July 2026

Published online: 23 July 2026

Check for updates

Yi Wu[1,5], Liyang Ma[2,5], Jianpeng Ao[2], Hanzhang Chen[1], Kuan Luo[2], Ting Wang[3,4] ✉, Minbiao Ji[2] ✉ & Xiaoyan Cui[1] ✉

Quantitatively tracking the dynamics of reactive species in vivo with reliable spatiotemporal resolution is essential yet challenging, as it provides critical insights into physiological mechanisms, optimizes drug delivery, and advances precision medicine. Herein, leveraging stimulated Raman scattering (SRS) for in vivo quantification, this work develops a series of versatile photoactivable scaffolds that efficiently generate equivalent amounts of reactive nitroxyl (HNO) and cyano-azobenzene with high photoconversion efficiency (95.1%) and fast reaction dynamics ($t_{1/2}$ = 3.97–33.56 s). Upon photoinduction, the cyano-azobenzene serves as a sensitive SRS imaging reporter, enabling precise monitoring of HNO release with high spatial resolution. Moreover, the modularly designed scaffolds ensure tuneable reaction kinetics and distinct vibrational fingerprints (2224–2245 cm^{-1}) for multiplexed SRS imaging, along with specified organelle-targeting capabilities. By tracking the photo-release of HNO in living cells and zebrafish using SRS imaging, we uncover kinetic lags in photo-triggered HNO, confirming its distinct spatiotemporal dynamics in complex living systems. Furthermore, this study monitors the therapeutic process of photoactivated HNO in a zebrafish model of heart failure using SRS, providing a robust strategy for quantifying reactive species in native biological environments.

Stimulated Raman scattering (SRS) microscopy is recognized as one of the most powerful tools in label-free bioimaging, utilizing significantly enhanced Raman vibrational transitions of chemical bonds via nonlinear effects[1–5]. Recently, the bursting of tailor-made SRS probes, designed by coupling strong vibrational tags, such as alkynes and nitriles, has further enabled the application of SRS microscopy with multi-channel and robust sensitivity in bioimaging[6–10]. Among the reported SRS probes, the pyronin-based Manhattan Raman scattering (MARS)[6] and polyyne-based 'carbon rainbow' (Carbow)[11] series are the star molecules with superb sensitivity and multiplicity. Their super-multiplexed and sharp Raman peaks from triple bonds within the cell-silent regions (1800–2800 cm^{-1}) ensured bioimaging without background signals from endogenous molecules[6,12]. Moreover, compared with spontaneous Raman scattering, SRS enables more efficient quantitative imaging due to the linear relationship between signal intensity and analyte concentration. This ensures precise spatiotemporal quantification, making SRS ideal for real-time tracking of drug delivery

[1]Department of Chemistry, School of Chemistry and Molecular Engineering, East China Normal University, Shanghai, China. [2]Department of Radiology, Huadong Hospital, Shanghai Key Laboratory of Clinical Geriatric Medicine, Shanghai Institute of Geriatrics and Gerontology, State Key Laboratory of Surface Physics and Department of Physics, Fudan University, Shanghai, China. [3]Shanghai Skin Disease Hospital, School of Medicine, Tongji University, Shanghai, China. [4]Shanghai Engineering Research Center of Topical Chinese Medicine, Shanghai, China. [5]These authors contributed equally: Yi Wu, Liyang Ma. ✉e-mail: wangting1983927@gmail.com; minbiaoj@fudan.edu.cn; xycui@chem.ecnu.edu.cn

and metabolic processes[13–17]. However, versatile SRS probes are still very limited.

Currently, two groups of photoactivable SRS probes have been reported in photo-triggered SRS imaging: reversible dithienylethene (DAE) for photoswitching[18,19] and caged cyclopropenone for multicolor imaging (Fig. 1a)[20]. However, SRS has mainly been used as an imaging strategy in these applications, despite its inherent advantages of instant, accurate quantification in noninvasive imaging not being fully exploited. In photo-controlled release, particularly in photo-controlled drug release, the ability to quantitatively track the released species in real time and with high spatial resolution is highly required. It ensures instant and accurate feedback activation, representing the ultimate goal of photo-triggered release, although this goal remains highly challenging with conventional imaging techniques[21–24].

Moreover, the instantaneous concentration of biomolecules, especially certain reactive molecules, is essential in their therapeutic processes. For example, nitroxyl (HNO)[25–28], the one-electron-reduced and protonated form of nitric oxide (NO^-), has great potential in cardiovascular, oncological, neurological, and immune-related diseases. In cardiomyocytes, HNO exerts potent positive inotropic and lusitropic effects by modulating the Ca^{2+} cycle through a distinct redox-dependent mechanism. It enhances RyR2 activity to facilitate sarcoplasmic reticulum Ca^{2+} release while simultaneously activating SERCA2a (via *atp2a2* disulfide formation) to accelerate Ca^{2+} reuptake. Concurrently, HNO exposure preserves the physiological expression of the Myl7 protein (encoded by the *myl7* gene), thereby sustaining downstream myofibrillar assembly and cardiac output[29–31]. To date, fluorescence-based probes have been extensively developed for the detection of HNO and have enabled important biological insights[32–34]. However, these approaches often suffer from photobleaching, limited quantitative accuracy, and spectral overlap in complex biological environments, which hinder their ability to accurately reflect real-time dynamic changes in biosystems. Spontaneous Raman imaging offers improved chemical specificity and inherent quantitative capability; however, its weak signal intensity limits its application in monitoring fast dynamic processes in living systems. Given these challenges, the intrinsic high reactivity and short lifetime of HNO further hamper accurate tracking of HNO concentration and dynamics in vivo[35–38]. Moreover, the effect of HNO is highly concentration-dependent: low levels act as signaling molecules, whereas high levels exert cytotoxic effects. Thus, dose-controlled and spatiotemporally precise release remains a vital topic in HNO-based therapeutic strategies.

Given the versatility of SRS in bioimaging and biomedicine, the design of easily manipulated multifunctional SRS probes is urgently needed. Here, we report a series of photoactivatable SRS probes for quantitatively tracking the instant release of bioactive HNO with robust spatiotemporal resolution in vivo. In the designed probes, the azo-benzonitrile scaffolds are masked with 1,2,4-oxadiazole-4-oxide (OXA)[39], which efficiently blocks the strong SRS signal from the cyanide group. Upon visible-light irradiation, the photoactivation of OXA released a nitrosyl intermediate, which rapidly yields benzoic acid and HNO (Fig. 1b)[35,40,41]. Meanwhile, the instantaneous formation of azo-benzonitrile ensured quantitative reporting of photoactivation via SRS imaging of the newly generated nitrile group.

The versatility of the azo-benzonitrile scaffold has ensured extensive structural diversity in the designed probes. Differently functionalized caging groups efficiently tune the photoactivities of the probes, while feasible structural decoration with organelle-targeting groups (mitochondria, lysosomes, and lipid droplets) ensures photoactivation and its dynamic monitoring at the subcellular level. Moreover, the robust photoactivity and kinetics ensure instantaneous release of HNO by the designed probes upon photoirradiation in living cells and zebrafish, enabling quantitative tracking of the photoactivation process via real-time SRS imaging. We quantitatively monitored the photo-triggered release of HNO-induced calcium dynamics in H9c2 cardiomyocytes and the therapeutic process in zebrafish heart failure models, observing abrupt changes in cytosolic Ca^{2+} levels and the subsequent restoration of heart rate. We have confirmed the feasibility and potential of SRS in photo-triggered drug release with designed SRS probes. Our efforts may spark a broad interest in the application of SRS in photo-triggered processes. Meanwhile, the developed azo-probes in this work offer a convenient molecular toolbox and approach for photo-triggered studies by SRS.

Azobenzene-based SRS scaffold

To systematically evaluate the potential of azobenzene as a high-performance SRS scaffold, we developed a palette of representative dyes (**1**–**5**) and validated their signal enhancement effects. Azobenzene has been recognized as an efficient Raman probe due to its strong resonance Raman enhancement and the quenching of intrinsic fluorescence. These unique properties make it highly advantageous for spontaneous Raman imaging, significantly boosting Raman signals in both the fingerprint and silent regions[42–44]. However, as SRS relies on nonlinear resonance, it remains uncertain whether the enhancement can be effectively translated to SRS applications. Five representative azobenzene dyes (**1**–**5**, see structures in Fig. 1b and properties in Table 1, S1) were synthesized via the diazotization coupling of 4-aminobenzonitrile and the corresponding aniline derivative, including 4-aminobenzonitrile (**1**), phenol (**2**), aniline (**3**), benzoyl chloride (**4**), and nitroso-benzene (**5**). 4-Aminobenzonitrile was converted into the corresponding diazonium salt upon treatment with sodium nitrite and subsequently subjected to Sandmeyer coupling reaction with aniline derivatives. Synthetic details and characterizations are available in the Electronic Supplementary Information (ESI).

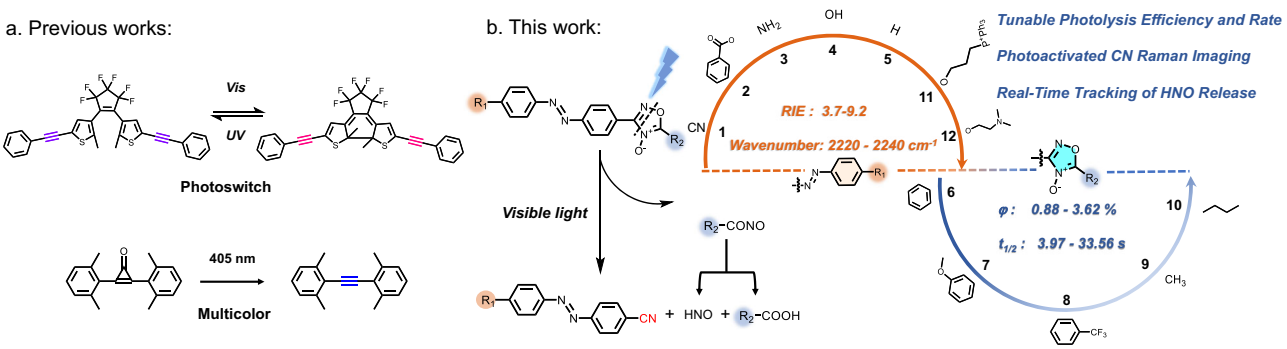

Fig. 1 | Design principles of photoactivatable probes for spatiotemporally controlled SRS imaging. a General strategies of photoactivatable fluorescent probes. Representative photoactivatable SRS probes based on carbon–carbon triple bond tags. Adapted from references[18–20]. **b** Strategy of photoactivatable azobenzene SRS probes utilizing cyano groups as vibrational reporters for real-time quantification.

Table 1 | Photophysical properties of compounds 1–5 and Ph-CN

Compound	1	2	3	4	5	Ph-CN
R_1	-CN	-OOC-Ph	$-NH_2$	-OH	-H	/
***Abs* (nm)**	337	331	365	346	341	224
RIE	9.2	3.7	5.3	5.1	4.6	0.15
Raman peak(cm^{-1})	2235	2234	2224	2229/2245	2231	2230

DFT calculations and experimental results confirm that the azobenzene scaffold significantly amplifies CN-stretching vibrations. Compounds **1**–**5** exhibited theoretical Raman activity (*S*) up to 2.8-5.6 folds higher than that of Ph-CN (Table S2). In SRS imaging, these probes showed strong signals (2220–2235 cm^{-1}) with RIE[45] values reaching 9.2 (*vs.* EdU (5-ethynyl-2′-deoxyuridine)). Remarkably, compound **5** achieved a ~32.4-fold enhancement in normalized SRS intensity compared to the nearly silent Ph-CN, demonstrating an efficient signal-boosting (Figs. S1, 2).

Electronic structures were fine-tuned for optimized optical performance. Compared to the compound **5** (RIE = 4.6), compounds **3** (-NH_2) and **4** (-OH) bearing electron-donating groups (EDGs) exhibited enhanced SRS signals (RIE: 5.1–5.3, Table 1). DFT and NBO analysis confirmed that EWGs increase bond polarization and k[46] (e.g., 19.01 mdyn/Å, $E^{(2)}$ = 20.11 kcal/mol, for **1**), whereas EDGs decrease k (18.82 mdyn/Å, $E^{(2)}$ = 20.97 kcal/mol for **3**), dictating the observed frequency shifts (Table S3 and Figs. S3, 4). Notably, the pH sensitivity of the phenolic group in **4** led to dual Raman peaks, potentially arising from the coexistence of protonated and deprotonated forms (Fig. S5). These results highlight electronic modulation as a robust strategy for tuning SRS frequency and intensity.

Azobenzene is a widely explored family with photo-triggered reversible isomerization[47,48]. Thus, the conformation and photostability of azobenzene-based SRS probes are essential. Herein, using **5** as the representative, we have confirmed that **5** predominantly (over 95%) exists in the transform by HPLC (Fig. S6). Upon repeated irradiation with intense UV (365 nm LED, 1.0 W/cm^2, 1 min) and visible light (425 nm LED, 50 mW/cm^2, 1 min), the instant and complete reversible *trans* − *cis* isomerization of **5** was confirmed by HPLC: **5** is isomerized from *trans*- into *cis*-form within 1 min (Fig. S7). In the SRS analysis, the isomerization is absent in the experimental conditions (pulse laser: 845 nm, 50 mW, Stokes laser: 1045 nm, 50 mW), or with visible light (LED, 425 nm, 50 mW/cm^2) within 2 h (Fig. S8a). Moreover, we confirmed that only the transform of **5** reports strong SRS signals (Fig. S8b). Considering the SRS signal intensity and synthesis feasibility for further functionalization, **5** was selected for further investigation.

In the spontaneous Raman spectra (10 mM DMSO solution of **5**, Fig. S9; 488 nm, 8.0 mW), the strong N = N stretching band at 1400–1500 cm^{-1} and the C ≡ N stretching vibration located in the cellular silent region are consistent with previously reported values. In contrast, the SRS spectrum of **5** exhibits a sharp and intense C ≡ N stretching vibration (Fig. S8b) with robust signal stability (Fig. S10), whereas the N = N double bond exhibits a complex peak pattern (Fig. S11). The precise vibrational position of the C ≡ N stretching mode was further confirmed by spontaneous Raman analysis. SRS intensities of the CN stretching band at 2231 cm^{-1} or **5** across a broad range of concentration (500 μM–100 mM) have demonstrated robust linear correlation with concentration (R^2 > 0.999; Fig. 2b). The corresponding limits of detection (LOD) and quantification (LOQ) by SRS were 51 μM and 169 μM, respectively, ~20.5-fold lower than those of benzonitrile (LOD = 1.05 mM, LOQ = 3.47 mM; Fig. 2c, S1, 12, and Table S4). These features enable reliable quantification over a broad dynamic range by SRS spectra and imaging[17]. Moreover, interference evaluation confirmed that the representative physiological ions (Na^+, K^+, Ca^{2+}, Mg^{2+}, Fe^{2+}, Zn^{2+}), biological reductants (GSH, Cys, Hcy), and reactive species (H_2O_2, $O_2^{\bullet-}$, $HO^{\bullet}$, $^1O_2$, $ONOO^-$, H_2S) have negligible impacts on the SRS response of **5** (Fig. S13a). Additionally, **5** exhibits strong stability across a wide pH range (2–12, Fig. S14).

Photo-triggered SRS scaffold

1,2,4-Oxadiazole-4-oxide (OXA)[49–52], a classical heteroaromatic scaffold, has recently emerged as a promising photochemical precursor[39,40,53,54]. Upon irradiation, OXA photolyzes in two steps: initial ring cleavage to benzonitrile and acyl nitroso, followed by a rapid and efficient transformation of the acyl nitroso intermediate into benzoic acid and nitroxyl (HNO, Fig. 1b)[26]. Moreover, the efficient conversion and rapid kinetics ensured OXA as one of the mildest and most reliable precursors for acyl nitroso species, a class of highly reactive intermediates[55]. Although extensive efforts have been devoted to tuning the kinetics of the subsequent transformation of acyl nitroso, the primary photoactivation remains poorly explored. Moreover, the application of OXA is limited by its long-criticized photoinstability. Herein, the formation of benzonitrile serves as an efficient turn-on strategy for photo-triggered SRS. Moreover, the proportionally generated -CN group and reactive HNO facilitated the quantitative monitoring of the instantaneous concentration of HNO by SRS intensities. With tuned reaction kinetics, the signal can be monitored in real time, ensuring controlled release with in situ visualization. Based on the azo- benzonitrile scaffold of **5**, 5-phenyl-3-(4-(phenyldiazenyl) phenyl)-1,2,4-oxadiazole 4-oxide (**6**) was synthesized. Starting from 4-carboxyazobenzene, sequential lithium aluminum hydride reduction afforded 4-(phenyldiazenyl) benzaldehyde, which was subsequently converted into the 4-phenyldiazenylbenzaldehyde oxime via oximation with hydroxylamine hydrochloride. The oxime was then oxidized to the reactive intermediate 4-azobenzene nitrile oxide, which underwent a 1,3-dipolar cycloaddition to afford 5-phenyl-3-(4-(phenyldiazenyl) phenyl)-1,2,4-oxadiazole-4-oxide (**6**). Derivatives **7**–**10** were synthesized by analogous procedures (details in ESI).

To understand the electronic modulation, DFT calculations were performed on the ground-state structures of **6**–**10**. The results showed that the substituents systematically tuned the N–O bond stability (Table S5) and the HOMO-LUMO gaps (Fig. 2a), leading to the observed differences in absorption spectra and photoreaction rates. Compared with direct laser-based regulation (Fig. S15), chemical manipulation provides intrinsic and predictable control over photoreaction kinetics, enabling efficient activation at lower irradiation intensities while minimizing phototoxicity in complex biological environments. Driven by diverse kinetics, a rapid intramolecular rearrangement leads to the stable formation of the CN-reporting unit (with a conversion efficiency of 96% at 5.0 mM, Fig. 2h and Table S6). The quantification of HNO by SRS relies on the 1:1 stoichiometric production of CN groups and HNO during the photo-reaction. In vitro HPLC trapping assays confirmed the stoichiometric relationship between azo-benzonitrile (**5**, 95.1%) and HNO (82.9%, n = 9, Figs. S16–19). Furthermore, the time-dependent generation of HNO was highly consistent with that of azo-benzonitrile in both in vitro environments and living cells (Figs. S18, 19).

Photoactivation of **6** was efficiently triggered by irradiation at wavelengths between 365 and 500 nm (LED, 50 mW/cm^2), although the reaction rate decreased with wavelength (Fig. 2d). The LED light sources were calibrated to the corresponding wavelengths (Fig. S20). The broad photo-sensitivity of **6** is consistent with the absorption of azobenzene and its characteristic n–π* transition (Fig. S21). 425 nm was selected for subsequent analysis. By contrast, the 3,5-diphenyl-1,2,4-oxadiazole 4-oxide showed negligible photo-reactivity with visible light (Fig. S22). HPLC confirmed the complete photoactivation of **6** (t_R = 13.2 min) to **5** (t_R = 14.3 min) and benzoic acid (t_R = 6.8 min) within 60 s (Fig. 2e). Taking 20 s as the interval, the fast photo-triggered reaction is vivid. UV–vis spectra further supported this transformation, as **6** (10 μM) exhibited a progressive shift from 355 to 341 nm under

https://doi.org/10.1038/s41467-026-75717-y

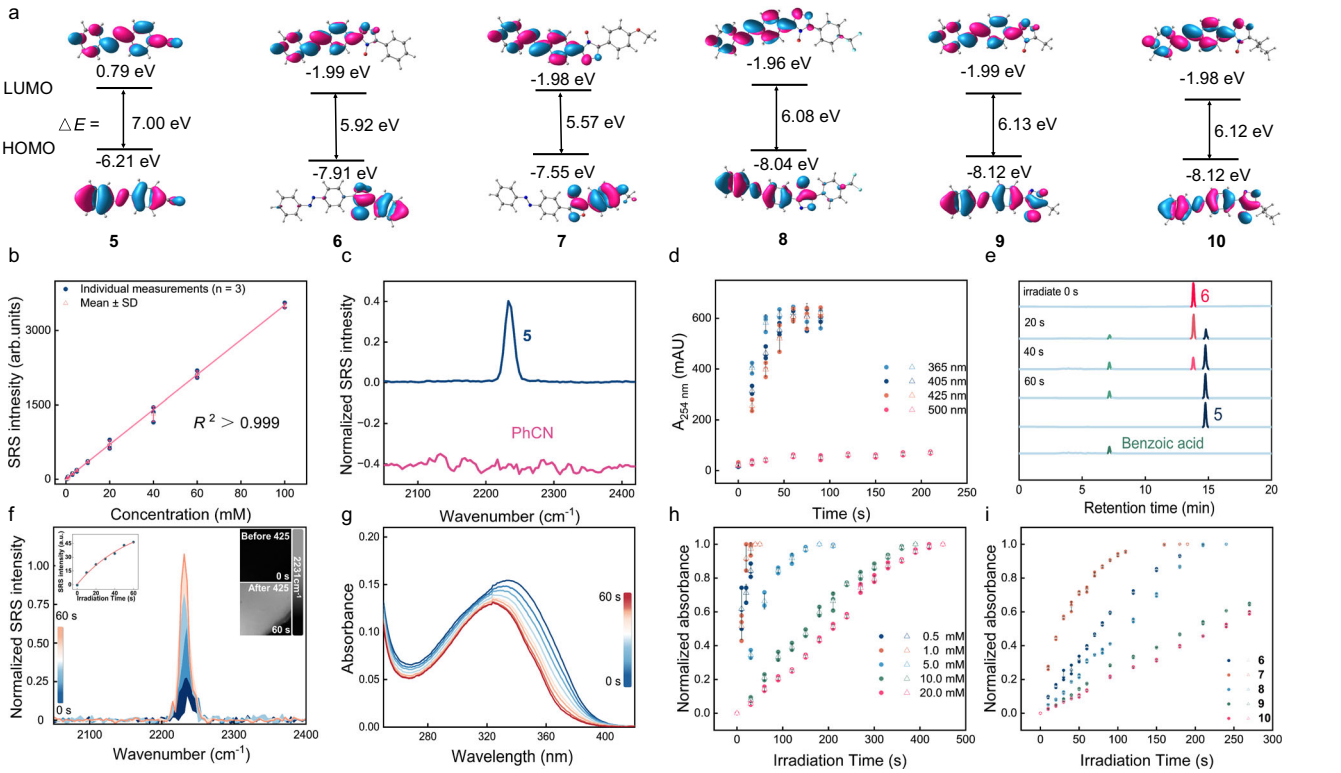

Fig. 2 | Photochemical properties and quantitative SRS analysis of photoactivatable probes. a Molecular orbitals and energies for **5**–**10**. **b** SRS signal intensity at 2231 cm^{-1} with the concentration of **5**. **c** SRS spectra for **5** and benzonitrile (10 mM in DMSO). **d** irradiating wavelength (365–500 nm) on the photoactivation of **6**. **e** HPLC for the photoactivation of **6**. **f** Temporal evolution of SRS spectra of **6** (10 mM in DMSO) with photo-irradiation (425 nm LED, 50 mW/cm^2). Inserts show the SRS images at 2231 cm^{-1} for solutions before and after irradiation, SRS intensities (I) and illumination time (t) follow $I = -71.8\exp(-t/58.8) + 72.3$, $R^2 = 0.993$. **g** Absorption spectra of **6** (15 μM in DMSO) during photoactivation. **h** HPLC-monitored absorption at 254 nm of **6** (0.5–20.0 mM in DMSO) with irradiation time. **i** The photoactivation of compounds **6**–**10**. Data are presented as mean ± SD from $n = 3$ independent replicates. Filled circles indicate individual data points, and open triangles indicate the mean values.

Table 2 | Photophysical properties of compounds 6–10

Compound	6	7	8	9	10
R_1	-H	-H	-H	-H	-H
R_2	-Ph	-Ph-OCH_3	-Ph-CF_3	-CH_3	-$(CH_2)_2CH_3$
***Abs* (nm)**	355	359	350	341	341
ε_{abs} ($M^{-1}cm^{-1}$)	12,578	13,649	12,654	11,548	11,669
φ (%)	1.88	3.62	1.24	0.96	0.88
$t_{1/2}$ (s)	11.91	3.97	17.78	29.45	33.56

irradiation (LED, 5.0 mW/cm^2), ultimately identical with the spectra of **5** (Fig. 2g). In addition, **6** demonstrated excellent stability toward physiological ions (Na^+, K^+, Ca^{2+}, Mg^{2+}, Fe^{2+}, Zn^{2+}), biological reductants (GSH, Cys, Hcy), and reactive species (H_2O_2, $O_2^{\bullet-}$, $HO^{\bullet}$, $^1O_2$, $ONOO^-$, H_2S) (Figure S13b). It also exhibited outstanding stability across a broad pH range (Fig. S23) and showed negligible decomposition within 48 h, even in concentrated GSH solutions (pH 7.4, Fig. S24). The robust photo-conversion of **6** at varying concentrations (100 μM–10 mM) was confirmed by HPLC: the conversion reached 96% at 5.0 mM and was approximately 86% at 20 mM (Fig. 2h, $n = 3$).

To further explore the photoreaction, compounds **7**–**10** were developed by structural decoration of **6** with anisole (**7**), (trifluoromethyl)benzene (**8**), methane (**9**), and butane (**10**) at the 4′-position. Initially, their photoreactions were confirmed by HPLC under 425 nm irradiation (Fig. 2I, 10 mM, LED, 50 mW/cm^2). Their photoreaction kinetics were calculated based on the SRS signals. Compound **7**, bearing an electron-donating methoxy group, exhibited the fastest reaction rate ($k_{obs} = 0.1741\ s^{-1}$, $t_{1/2} = 3.97$ s), followed by **6** ($k_{obs} = 0.0577\ s^{-1}$, $t_{1/2} = 11.91$ s) and **8** with the electron-donating moiety ($k_{obs} = 0.0592\ s^{-1}$, $t_{1/2} = 17.78$ s, 1.0 mM in DMSO, Table 1). Tuned electron-donating substituents efficiently manipulated the electron density of the N–O bond, thereby facilitating bond cleavage and promoting their photoactivation. In contrast, **9** and **10** with alkyl substitution showed slower rates ($k_{obs} = 0.0234\ s^{-1}$ and $0.0215\ s^{-1}$, respectively). Notably, both **9** and **10** exhibited nearly identical absorption spectra under photoirradiation, indicating minimal structural perturbations during photoactivation (Fig. S25). These five compounds had a tenfold difference in photoreaction rates, enabling their applications to meet diverse requirements. Meanwhile, DFT calculations were performed for the second-order perturbation energy ($E^{(2)}$) associated with electronic delocalization into the N–O antibonding orbital (σ^*)[56], as well as the variations in N–O bond length induced by substituents (Fig. S26 and Table S5). Additionally, different modifications resulted in varying photoreaction yields (φ from 0.88 to 3.62; Figs. S26, 27 and Table 2).

Time-resolved SRS spectra of photosensitive scaffold **6** show a gradual increase in intensity at 2231 cm^{-1} upon photoirradiation within 60 s (425 nm LED, 50 mW/cm^2 in DMSO), consistent with the formation of -CN during photoactivation. The photoactivation product is **5**, as confirmed by the SRS spectra and HPLC analysis (Fig. 2f). Kinetic analysis of the SRS signal evolution agreed with in vitro HPLC quantification ($I = -71.8e^{-t/58.8} + 72.3$, $R^2 > 0.99$), and the concentration quantified by SRS intensity (~ 8.3 mM) was consistent with that determined by HPLC.

Photoactivatable live-cell Raman imaging

Integrating an additional laser beam into the SRS system for photoactivation enables real-time and stable monitoring of probes in live

https://doi.org/10.1038/s41467-026-75717-y

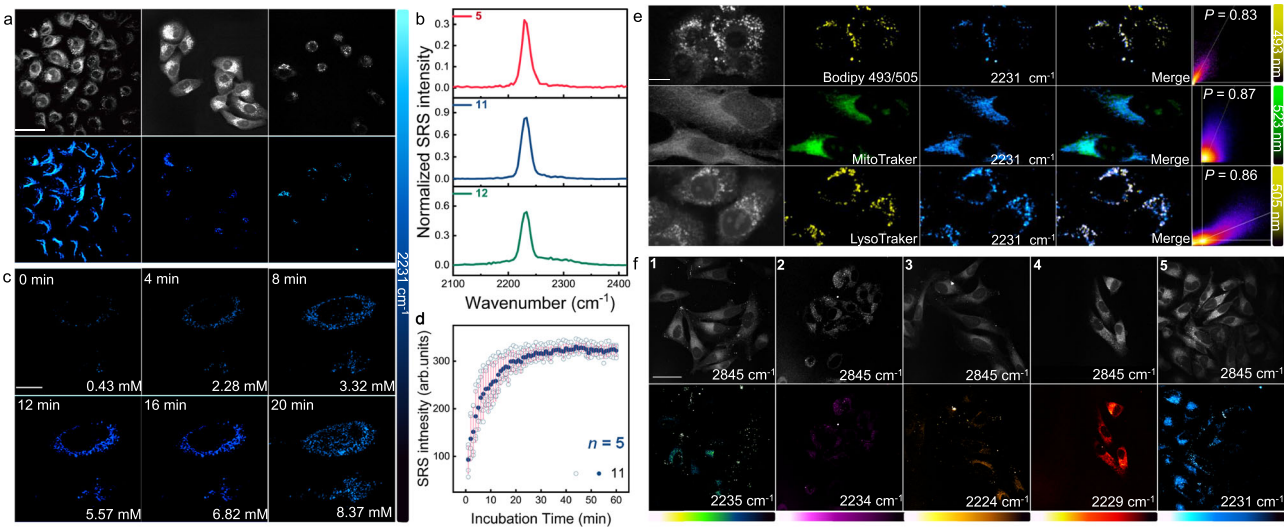

Fig. 3 | Organelle-targeted SRS imaging and cellular validation of photoactivatable nitrile probes. a SRS imaging of stained lipid droplets (**5**), mitochondria (**11**), and lysosomes (**12**) in HeLa cells; scale bar: 50 μm. **b** SRS spectra of **5, 11**, and **12** incubated in cells. **c** SRS imaging of **11** (40 μM)-stained HeLa cells at 0, 4, 8, 12, 16, and 20 min; scale bar: 10 μm. **d** SRS intensities of **11**-stained HeLa cells with the incubation time for randomly picked regions ($n = 5$, open circles indicate individual data points). **e** Colocalization of **5** (lipid droplets-targeted), **11** (mitochondria-targeted), and **12** (lysosome-targeted) with corresponding commercial fluorescent probes. Statistical significance of the correlation was determined using a two-sided Pearson correlation test. Scale bar: 10 μm. (**f**) SRS images of HeLa cells incubated with **1**–**5** at 2224–2235 cm^{-1}. Scale bar: 50 μm. Images are representative of three independent biological experiments with similar results.

cellular environments. To enable real-time and controllable photoactivation in live cells, we modified the instrument by splitting the excitation beam (845 nm) with a BBO frequency-doubling crystal to generate a 423 nm laser for photoactivation (Fig. S28). SRS imaging of **5**-stained live 3T3 cells (20 μM, 4 h) shows a strong signal at 2231 cm^{-1}. The SRS signal was stable with the SRS lasers on for 2 h. Additionally, at 20, 40, 60, and 80 min during SRS laser irradiation, the cells are additionally irradiated with a 423 nm pulse laser (0.50 mW) for 1 min without reducing the SRS signal (Fig. S29). In **6**-stained 3T3 cells (20 μM, 4 h), the SRS signal at 2231 cm^{-1} increased progressively upon 423 nm activation. (Fig. S30). Thus, the designed scaffold is a robust platform for photoactivation-guided SRS imaging in living cells.

Molecular engineering provides the probes with exceptional selectivity for stable organelle targeting and subcellular localization: **1**–**5** and their derivatives (photoactivatable probes) exhibited distinct SRS imaging signals within the 2224–2235 cm^{-1} range (Fig. 3f, S31, and Table S7). Among them, **5** was selected as the primary scaffold for further functionalization due to its superior biocompatibility and high synthetic yield. This foundational model enables the rational design of diverse organelle-targeted probes. A series of organelle-targeting probes was synthesized via the Ullmann reaction for the selective recognition of mitochondria (**11, 13**) and lysosomes (**12, 14, 15**, and **16**), featuring triphenyl phosphonium and dimethylamine groups at the para-position, respectively[57]. Probes with -CN (**11, 12**) and photo-caging oxadiazole-4-oxide (**13, 14, 15**, and **16**) are developed (Figs. 1, 4a). The intrinsic lipophilicity of **6** ensured its targeting to the lipid droplets. Co-localization analysis of the designed SRS probes with commercial markers for organelles, including Mito Tracker Green for mitochondria (Pearson correlation coefficient, $P = 0.87$ for **11**), Lyso Tracker Yellow HCK-123 for lysosomes ($P = 0.80$ for **12**), and Bodipy 493/503 for lipid droplets ($P = 0.83$ for **5**), demonstrated their reliable labeling specificity (Fig. 3e and Fig. S32). SRS spectra of the three targeted probes at 2231 cm^{-1} showed identical intensities, indicating the stability of the CN vibrational signal in complex organellar environments. The mitochondria-targeted **11** exhibited the fastest staining and strongest SRS signal (0.81 of the in vitro value in 20 min), followed by the lysosome-targeted **12** (0.33 in 2 h) and the lipid droplets-targeted probe **5** (0.12 in 6 h, Fig. 3a, b). Additionally, the dark toxicity and phototoxicity of different targeting probes (**6**–**14**) were assessed using the CCK-8 assay. The results indicated that, at the analyzed concentrations, these probes exhibited low toxicity (Figs. S33, 34).

Pulse-chase photoactivation experiments confirm the high spatiotemporal precision and minimal phototoxicity of the designed probes. The robust photosensitivity of SRS probes (**7, 13**, and **14**) in live cells is confirmed with pulse-chase photoactivation imaging. In **14**-stained live HeLa cells (20 μM, 2 h), SRS imaging of C–H vibrations at 2845 cm^{-1} (size: 212 × 212 μm) has vividly profiled cellular structures, confirming the biocompatibility of **14**. A 423 nm laser constantly irradiated a central region of interest (ROI, 106 × 106 μm) for 60 s (white dashed square in Fig. 4b) while capturing the SRS images (1 second/frame, s/f) at 2231 cm^{-1}. After irradiation for 10 s, SRS imaging at 2231 cm^{-1} resolved the lysosome only in the irradiated area. The SRS intensity increased rapidly, reached a constant level by 60 s, and kept the unirradiated region free of SRS vibration (Fig. 4b). Similarly, dynamic SRS imaging (1 s/f) at 2231 cm^{-1}. with pulse-chase photoactivation of selected ROI in **13**-stained HeLa cells (20 μM, 10 min) for mitochondria and **6**-stained 3T3 cells for lipid droplets (20 μM, 6 h, insulin and dexamethasone-induced, Fig. 4b). Additionally, **6** also demonstrated efficient photoactivation in Ac-LDL-induced J774A.1 cells (Fig. S35). Colocalization experiments further confirmed the excellent targeting properties of these photoactivated probes, with $P = 0.82$ for **6**, 0.86 for **13**, and 0.80 for **14** (Fig. S36). Notably, single-cell analysis of **14**-stained HeLa cells revealed a pronounced spectral contrast in the SRS profiles across the irradiated and non-irradiated regions (Fig. 4c, d and Supplementary Movie 1). By controlling the irradiation time across different areas (Fig. S37), we systematically compared the signals of the masked probes with those from directly incubated products (Fig. S38). Varying SRS intensities were generated within the same field of view, further proving the spatial precision and activation specificity of the designed strategy. The successful photoactivation across diverse cellular types and organelles confirmed the versatility and excellent spatiotemporal control of the designed strategy.

https://doi.org/10.1038/s41467-026-75717-y

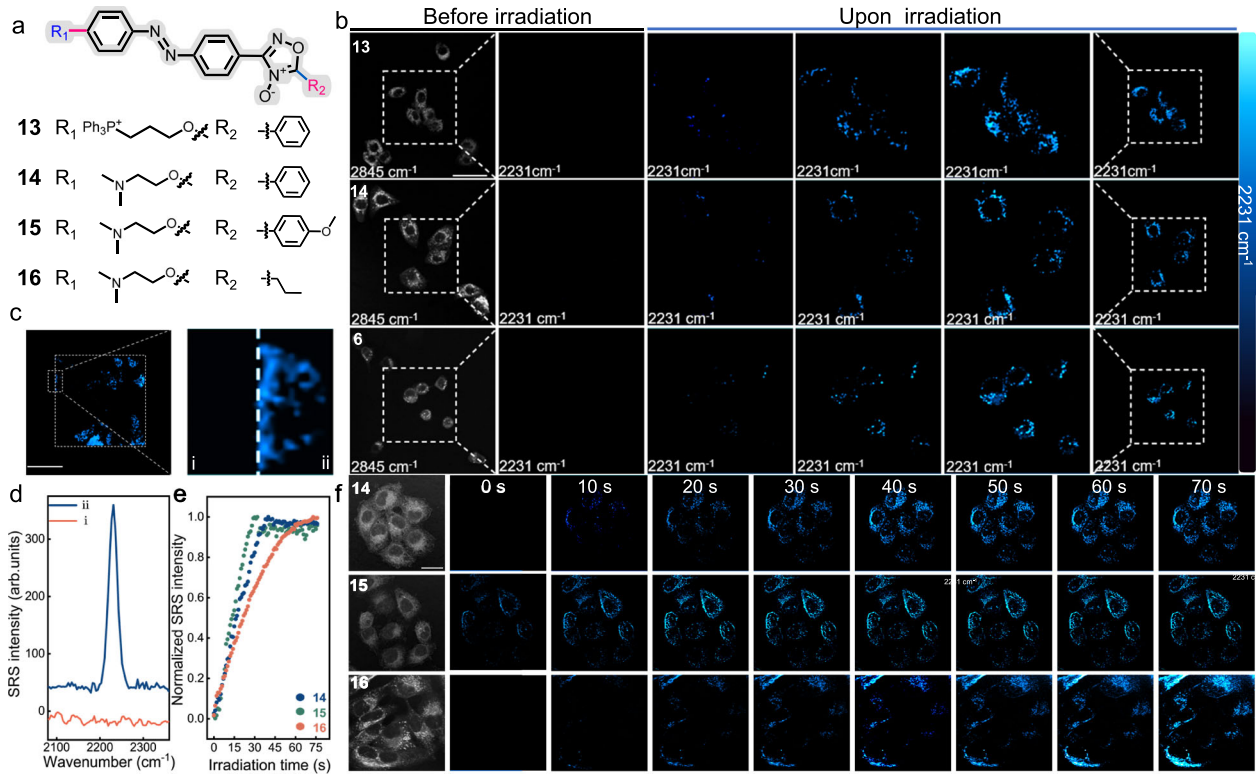

Fig. 4 | Spatiotemporally controlled photoactivation of nitrile SRS probes in living cells. a Structures of **13**–**16**. **b** SRS imaging of stained lipid droplets (**6**), mitochondria (**13**), and lysosomes (**14**) in live cells before (at 2845 cm^{-1}) and after (at 2231 cm^{-1}) localized irradiation (423 nm pulse laser, 0.5 mW) in the central regions; scale bar: 50 μm. Images are representative of three independent biological experiments. **c** SRS imaging of **14**-stained HeLa cells before and after localized irradiation; scale bar: 50 μm. SRS intensities of both the unirradiated (region 1) and irradiated (region 2) regions are enlarged, and SRS spectra in the corresponding regions are averaged in (**d**). **f** SRS imaging of **14**–**16** stained cells before and after irradiation in 70 s with 10 s as an interval; scale bar: 25 μm. **e** Averaged SRS intensities (1 s/f) of **14**–**16** stained cells after irradiation in 70 s.

The inherent quantifiability of SRS imaging facilitates precise tracking of cellular uptake kinetics, surpassing the limitations of conventional fluorescence techniques. Reliable real-time tracking of SRS intensities at the cellular level depends on the robust cellular permeability of the designed SRS probes. In **11**-stained HeLa cells (40 μM, 1 h, 53 × 53 μm), SRS imaging of C–H vibrations (2845 cm^{-1}, 53 × 53 μm) and delayed SRS imaging of CN vibrations in selected ROI (region 2) for HeLa cells revealed significant signals as early as the first frame, indicating its rapid membrane permeability and efficient cellular accumulation (Fig. 3c, Supplementary Movie 2). The SRS intensity of **13**-stained HeLa cells from selected ROIs ($n = 5$) indicated fast mitochondria labeling kinetics of the SRS probe. After staining, SRS intensity for -CN vibration rapidly accumulates in both the cytoplasm and mitochondria, and is uniformly distributed in the cytosol. After approximately 10 min, SRS intensity increased rapidly, indicating the reaching of mM-level concentrations. The SRS intensities increased linearly and then plateaued rapidly, reaching around 8.37 ± 0.02 mM (Fig. 3c). The uptake rate (k) constant was calculated as 0.19 ± 0.02 min^{-1}, and the half-life of the uptake process ($t_{1/2}$) was determined to be 3.65 ± 0.05 min^{-1} (Fig. 3d and S39). The kinetics are comparable to those of many mitochondrial fluorescence probes. Compared with fluorescence imaging[58,59], which typically suffers from nonlinearities and aggregation-caused quenching[60,61], SRS imaging allows for precise quantification even at high concentrations. Importantly, the distinct cyanide vibration at 2231 cm^{-1} in the Raman silent window ensured robust sensitivity and minimal interference for quantitative analysis.

We further explored the photo-triggered reaction rate in vivo by three lysosomal probes: **14, 15**, and **16** (Fig. 4a). These probes are, respectively, derived from **5, 7**, and **10**, photosensitive compounds with distinct kinetics for photoreaction. At identical experimental conditions, three probes displayed distinct kinetics for photoactivation in living cells: **14** exhibited a rapid photodecomposition reaction ($t_{1/2} = 27.5$ s), **15** showed a faster response ($t_{1/2} = 16.7$ s), while **16** was slower ($t_{1/2} = 42.7$ s, Figs. 4e, f), consistent with their reactivities in solution. These results highlight the versatility of this photoactivable SRS imaging strategy, which offers robust spatial and temporal precision. Moreover, the feasibly tunable reaction kinetics, achieved through rational molecular design, have further extended the potential of this strategy.

Photo-triggered HNO release in live cells

6 serves as a robust platform for the spatiotemporally controlled release of HNO, which can be quantitatively reported in real time via the synchronized SRS signal. In photo-triggered SRS imaging with designed probes, robust SRS signals are accompanied by the release of HNO, a reactive species with a proven therapeutic effect for heart failure, achieved through the controlled concentration of Ca^{2+}. However, the controlled release of HNO in vivo was hindered by its inherent instability, which resulted from rapid dimerization and reaction with thiols. Photo-triggered HNO release has been recognized as a promising strategy over conventional HNO donors, such as sodium trioxodinitrate (Angeli's salt)[62] and *N*-hydroxybenzenesulfonamide (Piloty's acid)[63]. With a reported phosphine-based hemicyanine fluorescent probe for HNO (**BHXP**)[31], the photo-triggered release of HNO in **6** was confirmed both in vitro (Fig. S40) and in living cells (Fig. S41). Notably, the HNO probe effectively captured HNO in both solution and cellular environments (compound **6**,

https://doi.org/10.1038/s41467-026-75717-y

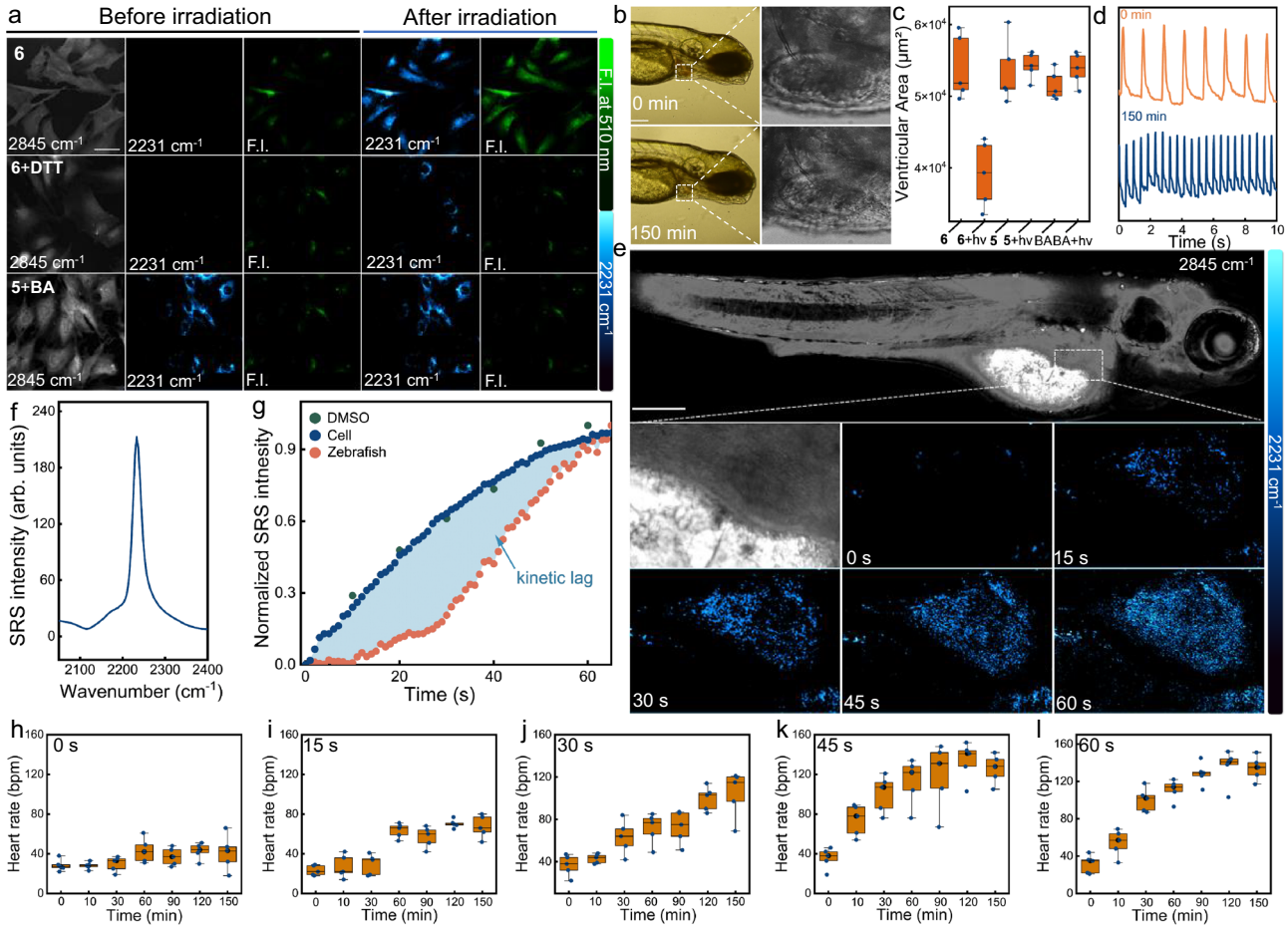

Fig. 5 | Photoactivated nitrile SRS imaging enables in vivo visualization and functional modulation of HNO signaling in a zebrafish heart failure model. **a** Fluo-4 AM (5.0 μM, 30 min)-stained H9c2 cells treated with **6** (20 μM, 4 h); **6** + DTT (100 μM, pretreated for 2 h); and **5** (20 μM, 4 h) + benzoic acid (20 μM, 4 h). SRS imaging at 2845 cm^{-1}, 2231 cm^{-1} and fluorescence at 510 nm were monitored before and after photoactivation. Scale bar: 50 μm. Images are representative of three independent biological experiments. **b** Ventricular of zebrafish with heart failure after incubation with **6** and photo irradiation at 0 min and 150 min, scale bar: 100 μm. **c** Ventricular areas of zebrafish embryos 4 h after treatment under different conditions: **6** in dark, **6** with *hv*, **5** in dark, **5** with *hv*, BA in dark, and BA with *hv*. **d** Image-based heart rate analysis of zebrafish during a 150 min recovery period. **e** SRS images of a zebrafish embryo at 2845 cm^{-1} and time-dependent SRS changes at 2231 cm^{-1} during photoactivation with pulse laser (423 nm, 0.5 mW), scale bar: 200 μm. **f** SRS spectra collected from **5** (20 μM, 4 h)-stained zebrafish. **g** SRS intensity at 2231 cm^{-1} during photoactivation in solution (10 mM, DMSO), live cells (20 μM, 4 h), and zebrafish (20 μM, 4 h). Heart rate for **6**-stained zebrafish embryos with heart failure after photoactivation (LED, 425 nm, 50 mW/cm^2) at **h** 0 s, **i** 15 s, **j** 30 s, **k** 45 s, and **l** 60 s; $n = 5$. In the box plots, the center line indicates the median; the box bounds represent the 25 and 75 percentiles; and the whiskers define the minimum and maximum values.

20 μM, irradiated with a 50 mW/cm^2 LED, 1 min), reaching equilibrium at 16 min in solution and 30 min in cells, consistent with previously reported findings. Furthermore, imaging of live cells using fluorescence and SRS also confirmed the photo-triggered generation of HNO (Fig. S42). In comparison, the real-time quantification of HNO by SRS offers a more precise monitoring of the instantaneous release of HNO. Except for HNO, the other products from the photoactivation of **6, 5** (20 μM) and benzoic acid (20 μM) induced insignificant fluorescence, further confirming the photo-triggered release of HNO by **6** in living cells (Fig. S38b).

The biological activity of the photo-released HNO was validated by its ability to rapidly release intracellular Ca^{2+} levels, particularly in cardiomyocytes. The upregulation of intracellular Ca^{2+} in H9c2 cardiomyoblast cells by photo-triggered HNO release is confirmed by Fluo-4AM[64,65], a commercial fluorescent Ca^{2+} probe. Significant fluorescence enhancement (~ 3.2-fold) was captured within 20 s of irradiation and immediately dropped to the baseline without irradiation in Fluo-4AM-stained H9c2 cells (Fig. 5a and S43). The dynamics of Ca^{2+} likely arise from HNO-mediated extracellular Ca^{2+} uptake or intracellular Ca^{2+} release[38,66]. Pretreatment with the HNO scavenger, dithiothreitol (DTT, 0.10 mM), has reduced the fluorescence intensities, confirming the involvement of HNO. A less profound elevation in Ca^{2+} in HeLa cells (1.4-fold) suggested the discrimination of cellular types in the HNO-mediated upregulation of Ca^{2+} (Fig. S44). Thus, SRS probe **6** serves as an efficient and controllable HNO donor, whose HNO release can be quantitatively reported by the SRS signal, offering a robust platform for photo-triggered release of reactive biomolecules in live organisms.

Treating heart-failed zebrafish with quantitatively monitored HNO release in vivo

Heart failure, a major cardiovascular disorder, is the inability of the heart to pump blood effectively to meet the demands of the body[67]. Recent advances highlight HNO as a promising therapeutic molecule for heart failure, likely due to its reversible modification of calcium-handling proteins[68,69]. Some photo-triggered HNO donors are designed for the controllable release of HNO[70–72]. However, the high reactivity and short lifetime of HNO have hindered the reliable quantification of HNO release in complex biological tissues in vivo. Photoactivation-based strategies offer an effective means to precisely control the spatiotemporal release of such reactive species. Verapamil-

treated Zebrafish embryos were employed as a representative vertebrate model of heart failure[73]. Herein, zebrafish embryos (3 dpf) incubated with verapamil (200 μM, 30 min) have resulted in significant ventricular enlargement and bradycardia. Compared with healthy zebrafish, the average ventricular area increased from (3.88 ± 0.46) $\times10^5$ μm^2 to (5.62 ± 0.37) $\times10^5$ μm^2, while the heart rate decreased from 148 ± 22 bpm to 51 ± 14 bpm (Fig. S45), suggesting the success in establishing a heart failure model in zebrafish.

Statistical analysis of heart rates and ventricular areas in zebrafish

Quantification of heart rate and ventricular area confirmed that the photo-triggered release of HNO effectively recovered cardiac function in heart-failure zebrafish. Zebrafish embryos with verapamil-induced heart failure were stained with **6** (20 μM, 4 h) or without **6** (control group), followed by photo irradiation (425 nm LED, 50 mW/cm^2, 1 min). The remarkable recovery in heart failure for **6**-stained zebrafish embryos was confirmed by increased heart rate from 53 ± 21 bpm to 132 ± 35 bpm 150 min after irradiation (Fig. 5b, d, n = 5). Meanwhile, the ventricular areas were decreased from (5.87 ± 0.73) $\times10^5$ μm^2 to (4.58 ± 0.84) $\times10^5$ μm^2 (n = 5). In contrast, zebrafish embryos in the control group, without staining by **6**, showed no sign of recovery at 150 min after irradiation (n = 5): The heart rate is 58 ± 19 bpm (0 min) and 46 ± 22 bpm (150 min); ventricular area is (5.66 ± 0.28) $\times10^5$ μm^2 (0 min) and (5.49 ± 0.54) $\times10^5$ μm^2 (150 min). We have also confirmed that the medication is not a product of photoactivation (**5** and benzoic acid). Since zebrafish embryos incubated with **5** and benzoic acid failed to recover: ventricular area: (5.94 ± 0.36) $\times10^5$ μm^2 (0 min) and (5.87 ± 0.48) $\times10^5$ μm^2 (150 min); heart rate: 48 ± 22 bpm (0 min) and 44 ± 18 bpm (150 min) (n = 5, Fig. 5c and S46). Thus, we confirmed that the photo-triggered release of HNO from **6** effectively ameliorates heart failure in zebrafish in vivo. In zebrafish embryos with heart failure co-incubated with the HNO scavenger, DTT (200 μM, 4 h), the heart rate was unaffected by photoirradiation (n = 5): 41 ± 12 bpm (0 min) and 35 ± 18 bpm (150 min). Removing DTT and re-incubating the embryos with **6** (20 μM, 4 h) and verapamil (200 μM, 30 min), photo irradiation (425 nm LED, 50 mW/cm^2, 1 min) led to a marked recovery of heart rate (n = 3, Fig. 5d and Fig. S47): 38 ± 17 bpm (0 min) and 122 ± 30 bpm (150 min). These findings confirmed the critical role of HNO in ameliorating heart failure. However, the spatiotemporal distribution of HNO in real time during the photo reaction remains unclear, and the effects of HNO on the therapeutic process of heart failure in zebrafish are still poorly understood due to the lack of quantitative analysis.

Real-time SRS imaging in live zebrafish revealed a distinct 'kinetic lag' in HNO release, highlighting the profound influence of the complex biological environments on photochemical dynamics. Herein, zebrafish embryos are incubated with **5** (20 μM, 4 h) and immobilized before whole-animal SRS imaging at dual vibrational modes (2231 and 2845 cm^{-1}). Robust SRS signals at 2231 cm^{-1} were observed in the zebrafish, and accumulated mainly at the abdomen, confirming the successful intake of **5** (Fig. S48). Zoom in to the abdomen, a sharp SRS peak at 2231 cm^{-1} suggested the intake of **5** (Fig. 5f). Then, a whole-body irradiation (423 nm, pulse laser: 0.5 mW/cm^2, 1 min) was applied to zebrafish embryos incubated with **6** (20 μM, 4 h), and strong SRS vibration at 2845 cm^{-1} has profiled the whole body of zebrafish (Fig. 5e and S49). After irradiation, the SRS signal at 2231 cm^{-1} for the CN vibration was increased rapidly and reached a plateau at 60 s in the abdomen (Fig. 5e). Notably, the classical ordered reaction in solution (Fig. 2f) was transformed into a quasi-autocatalytic reaction, characterized by a typical sigmoidal curve (Fig. 5g). Product formation is slow within the first 20 s; then a rapid rise in the SRS signal suggests accelerated formation of HNO between 20 and 60 s, after which the product concentration remains nearly constant at an estimated local concentration of ~5.7 mM. The distinct reaction profiles suggest different mechanisms for the photo-triggered release of HNO. Compared with photo-triggered release of HNO in solution or live cells in petri dishes, the vivid kinetic lag (dashed area in Fig. 5g) in the complex living zebrafish was quantitatively monitored by SRS imaging. The significantly distinct kinetic processes in different biological systems indicate the profound impact of biological factors on the dynamics of photo-triggered reactions in vivo.

To further evaluate the photo-triggered release of HNO and therapeutic processes in the biological system, **6**-stained zebrafish embryos with heart failure were subjected to photoirradiation for varying durations (0, 15, 30, 45, and 60 s). The corresponding heart rates were monitored after irradiation (0, 10, 30, 60, 90, 120, and 150 min) to quantify the dynamic recovery of the zebrafish with different amounts of HNO from irradiation (Fig. 5h–l). Without photoirradiation (0 s), the heart rates for **6**-stained zebrafish are around 42 ± 13 bpm. The heart rates of zebrafish with 15 s-irradiation started to increase after 60-min incubation, suggesting their slow recovery, although the heart rates increased to 81 ± 26 bpm, failed to achieve full recovery. Zebrafish with 30 s-irradiation got fully recovered (heart rate: 121 ± 22 bpm) at 150 min, although the heart rates started to increase after 30 min. For zebrafish with 45 or 60 s-irradiation, the released HNO started to show therapeutic effects at 10 min and enabled full recovery at 90 min-incubation to the same level as that of normal zebrafish (heart rates: 129 ± 17 and 138 ± 26 bpm, respectively), suggesting the dose-related therapeutic process in HNO-treated heart failure. Statistical analysis of heart rates at 30 min post-irradiation showed that HNO treatment for heart failure is consistent with the photo-triggered dynamic release of HNO, as quantitatively monitored with SRS (Figs. S50–S55). To further evaluate the dose-dependent recoveries in zebrafish, quantitative RT-PCR analysis in three groups of zebrafish (heart failure group, photo-triggered HNO-treated group, and control group) confirmed that the photo-triggered release of HNO significantly rescued the verapamil-induced transcriptional derangement, restoring *atp2a2* (from 1.00 ± 0.03 to 1.14 ± 0.03) and *myl7* expression (from 1.00 ± 0.06 to 1.68 ± 0.04) in the heart regions of 3 dpf zebrafish (Fig. S56).

Herein, the dose-response evaluation in zebrafish has established the relationship between HNO concentration and cardiac function. We conclude that, in the treatment of heart failure with photo-triggered HNO release, HNO at different concentrations exhibits distinct therapeutic dynamics, as quantitatively confirmed by SRS. The analysis is essential for precise dosing and controlled release of reactive HNO, ensuring the optimal dosing and therapeutic time window and achieving maximum efficacy with minimal side effects. To the best of our knowledge, this is the first report of SRS imaging of zebrafish in the cellular silent region. Quantitative monitoring of photo-triggered HNO release in zebrafish using SRS imaging has confirmed the rapid dynamics of HNO, facilitating further photo-triggered non-invasive treatment of heart failure.

Tracking the dynamics of active species in vivo is highly challenging but eagerly desired by scientists across various fields. SRS imaging is an efficient strategy for quantitatively monitoring the dynamics of reactive species in live biological systems with robust spatiotemporal resolution. In this work, we established a modular probe palette with diverse reaction kinetics and vibrational frequencies, serving as a versatile library for multicolor imaging and applications in complex physiological environments. Crucially, manipulating their release kinetics has ensured efficient activation, avoiding potential photodamage. By developing a group of photoactivable SRS probes that can form HNO and cyanide of equivalent molar quantities upon photo-irradiation, we were able to track the photoreaction and the instantaneous concentration of HNO by analyzing the SRS intensity from the cyanide in vivo. The kinetic lag for the release of HNO in zebrafish has suggested distinct photoreaction kinetics in complex biological systems compared with those in solution or dispersed cells in petri dishes. Moreover,

the physiological response of zebrafish with heart failure has confirmed that the biological effects of HNO are dose-dependent. These results are essential in the design of HNO prodrugs and the therapeutic process involving the controlled release of HNO. Moreover, the modular strategy provides a versatile platform for photoactivatable SRS probes that are capable of releasing a wide range of therapeutic agents or reactive species with tunable kinetics. When combined with quantitative in vivo SRS imaging, it enables high-spatiotemporal-resolution studies of dynamic chemical processes in living systems. We believe this platform can facilitate the study of reactive species signaling and metabolic pathways, and support the development of precision therapeutic strategies, offering novel tools and opportunities for both fundamental research and biomedical applications.

Methods

Chemical synthesis

Compounds **1**–**5** were synthesized via a standard diazonium coupling procedure. Briefly, the corresponding substituted anilines were treated with sodium nitrite in an aqueous hydrochloric acid solution at 0 °C to generate diazonium salts. Subsequently, these intermediates were reacted with electron-rich aromatic coupling partners in ethanol at 0 °C–5 °C to yield the desired azo derivatives. Compounds **6**–**10** were synthesized via a [3 + 2] cycloaddition reaction. Briefly, (*E*) -4-((*E*)-phenyldiazenyl) benzaldehyde oxime was treated with HClO in a mixture of methanol and dichloromethane to generate the corresponding nitrile oxide in situ. Subsequent addition of various enamines (2–5 equiv.) enabled cyclization, affording the target products.

Stimulated Raman scattering and microscopy

An integrated laser system (femtosecond optical parametric oscillator, Insight X3 + , Newport) served as the excitation source for both the pump and Stokes beams. This system produced a ~ 150 fs pump pulse tunable from 690 to 1300 nm and a fixed 1045 nm Stokes pulse at an 80 MHz repetition rate. The Stokes beam was modulated at 20 MHz using an electro-optic modulator. To achieve spectral resolution, both beams were temporally stretched into the picosecond regime using SF57 glass rods. After spatial and temporal synchronization, the beams were directed into an inverted multi-photon laser scanning microscope (FV3000, Olympus) and focused onto the sample through a 60× water-immersion objective lens (Olympus, UPLSAPO 60×W, NA 1.2).

Reporting summary

Further information on research design is available in the Nature Portfolio Reporting Summary linked to this article.

Data availability

In alignment with the guidelines, our newly developed small-molecule probes fully meet the required criteria for target selectivity, potency, and mechanism of action. the chemical, optical, and bio-imaging data generated in this study are provided in the Supplementary Information/Source Data file. Source data are provided with this paper.

References

1. Freudiger, C. W., Min, W., Saar, B. G. & Lu, S. Label-free biomedical imaging with high sensitivity by stimulated Raman scattering microscopy. *Science* **322**, 1857–1860 (2008).
2. Lu, F.-K. et al. Label-free DNA imaging in vivo with stimulated Raman scattering microscopy. *Proc. Natl. Acad. Sci. USA* **112**, 11624–11629 (2015).
3. Tipping, W. J. et al. Stimulated Raman scattering microscopy: an emerging tool for drug discovery. *Chem. Soc. Rev.* **45**, 2075–2089 (2016).
4. Hu, F., Shi, L. & Min, W. Biological imaging of chemical bonds by stimulated Raman scattering microscopy. *Nat. Methods* **16**, 830–842 (2019).
5. Lin, H. et al. Label-free nanoscopy of cell metabolism by ultrasensitive reweighted visible stimulated Raman scattering. *Nat. Methods* **22**, 1040–1050 (2025).
6. Wei, L. et al. Super-multiplex vibrational imaging. *Nature* **544**, 465–470 (2017).
7. Fujioka, H. et al. Multicolor activatable Raman probes for simultaneous detection of plural enzyme activities. *J. Am. Chem. Soc.* **142**, 20701–20707 (2020).
8. Jiang, Y. et al. An activity-based sensing approach to multiplex mapping of labile copper pools by stimulated Raman scattering. *J. Am. Chem. Soc.* **146**, 33324–33337 (2024).
9. Fujioka, H. et al. Activatable Raman probes utilizing enzyme-induced aggregate formation for selective ex vivo imaging. *J. Am. Chem. Soc.* **145**, 8871–8881 (2023).
10. Tian, S. et al. Polydiacetylene-based ultrastrong bioorthogonal Raman probes for targeted live-cell Raman imaging. *Nat. Commun.* **11**, 1–9 (2020).
11. Hu, F. et al. Supermultiplexed optical imaging and barcoding with engineered polyynes. *Nat. Methods* **15**, 194–200 (2018).
12. Suzuki, Y. et al. Label-free chemical imaging flow cytometry by high-speed multicolor stimulated Raman scattering. *Proc. Natl. Acad. Sci. USA* **116**, 15842–15848 (2019).
13. Fu, D. et al. Quantitative chemical imaging with multiplex stimulated Raman scattering microscopy. *J. Am. Chem. Soc.* **134**, 3623–3626 (2012).
14. Fu, D. Quantitative chemical imaging with stimulated Raman scattering microscopy. *Curr. Opin. Chem. Biol.* **39**, 24–31 (2017).
15. Figueroa, B. et al. Quantitative imaging of intracellular density with ratiometric stimulated Raman scattering microscopy. *J. Phys. Chem. B.* **126**, 7595–7603 (2022).
16. Zhang, D. et al. Quantitative vibrational imaging by hyperspectral stimulated Raman scattering microscopy and multivariate curve resolution analysis. *Anal. Chem.* **85**, 98–106 (2012).
17. Fu, D. et al. Imaging the intracellular distribution of tyrosine kinase inhibitors in living cells with quantitative hyperspectral stimulated Raman scattering. *Nat. Chem.* **6**, 614–622 (2014).
18. Ao, J. et al. Switchable stimulated Raman scattering microscopy with photochromic vibrational probes. *Nat. Commun.* **12**, 3089 (2021).
19. Yang, Y., Bai, X. & Hu, F. Photoswitchable polyynes for multiplexed stimulated Raman scattering microscopy with reversible light control. *Nat. Commun.* **15**, 2578 (2024).
20. Du, J. & Wei, L. Multicolor photoactivatable Raman probes for subcellular imaging and tracking by cyclopropenone caging. *J. Am. Chem. Soc.* **144**, 777–786 (2021).
21. Brieke, C. et al. Light-controlled tools. *Angew. Chem. Int. Ed.* **51**, 8446–8476 (2012).
22. Weinstain, R. et al. Visible-to-NIR-light activated release: from small molecules to nanomaterials. *Chem. Rev.* **120**, 13135–13272 (2020).
23. Klán, P. et al. Photoremovable protecting groups in chemistry and biology: reaction mechanisms and efficacy. *Chem. Rev.* **113**, 119–191 (2012).
24. Hüll, K., Morstein, J. & Trauner, D. In vivo photopharmacology. *Chem. Rev.* **118**, 10710–10747 (2018).
25. Miranda, K. M. The chemistry of nitroxyl (HNO) and implications in biology. *Coord. Chem. Rev.* **249**, 433–455 (2005).
26. Sabbah, H. N. et al. Nitroxyl (HNO): a novel approach for the acute treatment of heart failure. *Circ. Heart Fail.* **6**, 1250–1258 (2013).
27. Arcaro, A., Lembo, G. & Tocchetti, C. G. Nitroxyl (HNO) for treatment of acute heart failure. *Circ. Heart Fail.* **11**, 227–235 (2014).
28. Tocchetti, C. G. et al. Playing with cardiac "redox switches": the "HNO way" to modulate cardiac function. *Antioxid. Redox Signal.* **14**, 1687–1698 (2011).
29. Parissis, J. et al. Nitroxyl donors for acute heart failure: promising newcomers. *Eur. J. Heart Fail.* **19**, 1333–1334 (2017).

30. McCarthy, E. et al. Oxidative and hydrolytic HNO formation from a clinical drug hydroxyurea catalyzed by horseradish peroxidase: basic mechanism, active site effect and implications for drug design. *JACS Au* **5**, 2849–2860 (2025).
31. Chai, Z. et al. A tumor-targeted near-infrared fluorescent probe for HNO and its application to the real-time monitoring of HNO release in vivo. *Chem. Commun.* **57**, 5063–5066 (2021).
32. Shi, Y. & Zhang, Y. Mechanisms of HNO reactions with ferric heme proteins. *Angew. Chem. Int. Ed.* **57**, 12490–12494 (2018).
33. Rivera-Fuentes, P. & Lippard, S. J. Metal-based optical probes for live cell imaging of nitroxyl (HNO). *Acc. Chem. Res.* **46**, 420–432 (2013).
34. Yue, X. et al. Mitochondria-targeted fluorescent probe for super-resolution imaging of HNO in lung cancer. *Anal. Chem.* **89**, 2015–2021 (2017).
35. Augustyniak, A., Skrzypek, J. & Błaszczyk, A. Cytotoxicity of nitroxyl (HNO/NO^-) against normal and cancer human cells. *Chem. Biol. Interact.* **206**, 262–271 (2013).
36. Hewett, S. J. et al. Neurotoxicity of nitroxyl: insights into HNO and NO biochemical imbalance. *Free Radic. Biol. Med.* **39**, 1478–1488 (2005).
37. Smulik, R. et al. Nitroxyl (HNO) reacts with molecular oxygen and forms peroxynitrite at physiological pH: biological implications. *J. Biol. Chem.* **289**, 35570–35581 (2014).
38. Najjar, R. S. et al. Nitroxyl protects H9c2 cells from H/R-induced damage and inhibits autophagy via PI3K/Akt/mTOR pathway. *PLoS One* **20**, e0314500 (2025).
39. Quadrelli, P. et al. Photochemical generation of nitrosocarbonyl intermediates on solid phase: synthons toward hetero Diels–Alder and ene adducts through photocleavage. *J. Comb. Chem.* **7**, 887–892 (2005).
40. Maimon, E. et al. Direct observation of acyl nitroso compounds in aqueous solution and the kinetics of their reactions with amines, thiols and hydroxamic acids. *J. Phys. Chem. A.* **122**, 7006–7013 (2018).
41. Cohen, A. D. et al. Direct observation of an acyl nitroso species in solution by time-resolved IR spectroscopy. *J. Am. Chem. Soc.* **125**, 1444–1445 (2003).
42. Tang, Y. et al. Azo-enhanced Raman scattering for enhancing the sensitivity and tuning the frequency of molecular vibrations. *ACS Cent. Sci.* **7**, 768–780 (2021).
43. Ma, W. et al. Azo-enhanced Raman scattering probing proton transfer between water and nanoscale zero-valent iron. *J. Am. Chem. Soc.* **146**, 32785–32794 (2024).
44. Yu, Y. et al. High-resolution low-power hyperspectral line-scan imaging of fast cellular dynamics using azo-enhanced Raman scattering probes. *J. Am. Chem. Soc.* **144**, 15314–15323 (2022).
45. Dodo, K. et al. Alkyne-tag Raman imaging and sensing of bioactive compounds. *Nat. Rev. Methods Prim.* **5**, 1 (2025).
46. Hoffman, A. E. J. et al. A critical assessment on calculating vibrational spectra in nanostructured materials. *J. Chem. Theory Comput.* **20**, 513–531 (2023).
47. Zhou, H. et al. Photoswitching of glass transition temperatures of azobenzene-containing polymers induces reversible solid-to-liquid transitions. *Nat. Chem.* **9**, 145–151 (2017).
48. Nie, H. et al. Switchable reversible addition–fragmentation chain transfer (RAFT) polymerization with the assistance of azobenzenes. *Angew. Chem. Int. Ed.* **58**, 11449–11453 (2019).
49. Quadrelli, P., Milanese, M. & Caramella, P. A photochemical generation of nitrosocarbonyl intermediates. *Tetrahedron Lett.* **40**, 797–800 (1999).
50. Quadrelli, P. et al. Cycloadditions of nitrile oxides to amidoximes: a general synthesis of 3,5-disubstituted 1,2,4-oxadiazole-4-oxides. *Tetrahedron Lett.* **53**, 1787–1796 (1997).
51. De Sarlo, F. & Giacomelli, A. Behaviour of nitrile oxides towards nucleophiles. Part III. Dimerisation of aromatic nitrile oxides catalysed by trimethylamine. *J. Chem. Soc. Perkin Trans. 1* **17**, 1825–1827 (1976).
52. Pace, A. et al. Molecular rearrangements of 1-oxa-2-azoles as an expedient route to fluorinated heterocyclic compounds. *Heterocycles* **63**, 2627–2648 (2004).
53. Bodnar, B. S. & Miller, M. J. The nitrosocarbonyl hetero-Diels–Alder reaction as a useful tool for organic syntheses. *Angew. Chem. Int. Ed.* **50**, 5630–5647.51 (2011).
54. Memeo, M. G. & Quadrelli, P. Generation and trapping of nitrosocarbonyl intermediates. *Chem. Rev.* **117**, 2108–2200 (2017).
55. Memeo, M. G. et al. HNO made easy from photochemical cycloreversion of novel 3,5-heterocyclic disubstituted 1,2,4-oxadiazole-4-oxides. *Tetrahedron Lett.* **69**, 7387–7394 (2013).
56. Alabugin, I. V. & Zeidan, T. A. Stereoelectronic effects and general trends in hyperconjugative acceptor ability of σ bonds. *J. Am. Chem. Soc.* **124**, 2729–2759 (2002).
57. Akhtar, R. et al. Recent green synthetic approaches toward Ullmann reaction: a review. *Chem. Pap.* **76**, 7275–7293 (2022).
58. Sajid, A. et al. Reversing the direction of drug transport mediated by the human multidrug transporter P-glycoprotein. *Proc. Natl. Acad. Sci. USA* **117**, 29609–29617 (2020).
59. Irion, G. O. et al. Kinetics of vital staining of mitochondria in HeLa cells with lipophilic cationic fluorescent dyes. *Histochemistry* **99**, 75–83 (1993).
60. Lu, F. & Yuan, Y. A flexible chamber for time-lapse live-cell imaging with stimulated Raman scattering microscopy. *J. Vis. Exp.* **186**, e64045 (2022).
61. Li, X. et al. Mitochondrial imaging with combined fluorescence and stimulated Raman scattering microscopy using a probe of the aggregation-induced emission characteristic. *J. Am. Chem. Soc.* **139**, 17022–17030 (2017).
62. Zarpelon, A. C. et al. The nitroxyl donor, Angeli's salt, inhibits inflammatory hyperalgesia in rats. *Neuropharmacology* **71**, 1–9 (2013).
63. Adas, S. K. et al. Synthesis and HNO-donating properties of the Piloty's acid analogue trifluoromethanesulfonyl hydroxamic acid: evidence for quantitative release of HNO at neutral pH conditions. *Chem. Eur. J.* **24**, 7330–7334 (2018).
64. Lax, A., Santos, F. & Ferná ndez-Belda, F. Cytoplasmic Ca^{2+} signals and cellular death by apoptosis in myocardiac H9c2 cells. *Biochim. Biophys. Acta Mol. Cell Res.* **1763**, 937–947 (2006).
65. Lu, B. et al. Mitochondrial calcium homeostasis mediated by estradiol contributes to atrial fibrillation protection. *Biochem. Biophys. Res. Commun.* **772**, 1–7 (2025).
66. Tocchetti, C. G. et al. Nitroxyl improves cellular heart function by directly enhancing cardiac sarcoplasmic reticulum Ca^{2+} cycling. *Circ. Res.* **100**, 96–104 (2007).
67. Narumanchi, S. et al. Zebrafish heart failure models. *Front. Cell Dev. Biol.* **9**, 662583 (2021).
68. Mundina-Weilenmann, C. B. & Mattiazzi, A. Tracking nitroxyl-derived posttranslational modifications of phospholamban in cardiac myocytes. *J. Gen. Physiol.* **151**, 718–721 (2019).
69. Njegic, A., Wilson, C. & Cartwright, E. J. Targeting Ca^{2+} handling proteins for the treatment of heart failure and arrhythmias. *Front. Physiol.* **11**, 1068 (2020).
70. Zhou, Y.-C. et al. Rapid photoactivated generation of nitroxyl (HNO) under neutral pH conditions. *Angew. Chem. Int. Ed.* **55**, 13229–13232 (2016).
71. Kawaguchi, M. et al. Development and cellular application of visible-light-controllable HNO releasers based on caged Piloty's acid. *Chem. Commun.* **54**, 10371–10374 (2018).
72. Saha, S. et al. Photo-induced nitroxyl anion/HNO release from a nitrosyl complex of Mn(II)–porphyrinate. *Chem. Commun.* **61**, 2353–2356 (2025).

73. Zhu, X.-Y. et al. A zebrafish heart failure model for assessing therapeutic agents. *Zebrafish* **15**, 243–253 (2018).

Acknowledgements

The authors thank Dr. Weikang Wang from the Material Characterization Center at East China Normal University for technical assistance (ECNUIIP2026-07).

Author contributions

Y.W. and L.M. contributed equally. Y.W. contributed to the synthesis and analysis. Y.W., L.M., J.A., and K.L. contributed to the SRS imaging; Y.W. and H.C. contributed to the zebrafish experiments. T.W., M.J., and X.C. designed and supervised the whole project. The manuscript was written through the contributions of all authors. All authors have given approval to the final version of the manuscript.

Funding

This work was supported by the National Key R&D Program of China (2025YFF0517900 by M.J.) and the National Natural Science Foundation of China (Nos. 22374163 by T.W.; 22274056 and 22574055 by X.C.; 62425501 by M.J.). This work was also supported by the Fundamental Research Funds for the Central Universities.

Competing interests

The authors declare no competing interests.

Additional information

Supplementary information The online version contains supplementary material available at https://doi.org/10.1038/s41467-026-75717-y.

Correspondence and requests for materials should be addressed to Ting Wang, Minbiao Ji or Xiaoyan Cui.

Peer review information *Nature Communications* thanks Yasuyuki Ozeki, Tingjuan Gao and Huseyin C. Yalcin for their contribution to the peer review of this work. A peer review file is available.